

Radiation-enhanced nanobubble therapy: Monitoring treatment effects using photoacoustic imaging

Eno Hysi^{1,2}, Muhannad N. Fadhel^{1,2}, Anoja Giles^{3,4}, Yanjie Wang^{1,2}, Joseph A. Sebastian^{1,2}
Gregory J. Czarnota^{3,4}, Agata A. Exner⁵, Michael C. Kolios^{1,2,*}

¹Department of Physics, Ryerson University, Toronto, Canada; ²Institute for Biomedical Engineering, Science and Technology, St. Michael's Hospital, Toronto, Canada; ³Physical Sciences, Sunnybrook Research Institute, Toronto, Canada; ⁴Radiation Oncology, Sunnybrook Health Sciences Center, Toronto, Canada; ⁵Department of Radiology, Case Western Reserve University, Cleveland, United States

*mkolios@ryerson.ca

Abstract—In this work we demonstrate the potential of using nanobubbles (NBs) as radiation therapy enhancers for maximizing tumoral cell death. Photoacoustic (PA) imaging can be used to probe the mechanism of action of this treatment due to its ability to examine the oxygenation of tumors. *In vivo* experiments were performed in mice bearing prostate cancer tumors and the NB therapies were compared with conventional microbubble (MB) treatments combined with radiation. Our preliminary results show that NB combined with a single dose of 8 Gy radiation induce 40% tumor cell death compared to 20% observed with MB treatments. PA imaging suggest that NBs have an extravascular effect.

Keywords—nanobubbles, microbubbles, radiation therapy, photoacoustic imaging, tumor oxygenation, vascular disruption

I. INTRODUCTION

Since their first introduction in 1968, ultrasound contrast agents have expanded the diagnostic capabilities of ultrasound imaging [1]. Over half a century later, the interest in using microbubbles (MBs) for addressing relevant problems in biomedicine extends beyond their well-known contrast-enhancing capabilities. Clinically available contrast agents are typically 1-10 μm in diameter, allowing them to remain intravascular [2]. From a therapeutic perspective, the size limitation makes them ideal vascular targeted agents. When exposed to acoustic fields inducing stable cavitation, MBs have been shown to cause reversible endothelium permeability and local drug release [3]. On the other hand, the inertial cavitation of gas filled MBs results in irreversible mechanical and physical changes to the surrounding environment. Such a strategy has been used to increase vascular permeability amplifying the release of therapeutic payload to tumors [4], inducing thrombolysis of blood clots [5] and leading to localized opening of the blood brain barrier [6] for chemotherapeutic, gene or immunotherapies.

Czarnota and colleagues demonstrated in 2012 that combination of radiotherapy with ultrasound-driven microbubble cavitation acts as an effective radiation-enhancing treatment [7]. MB therapy combined with radiation causes endothelial cell death and vascular disruption of tumor blood vessels with supra-additive DNA damage of cancer cells *in vivo* [8]. The synergistic effects of combining a single treatment of ultrasound-simulated MB vascular perturbation with radiation induces over 10-fold increase in cellular kill. Despite these promising advances, a major limitation of any MB-based treatment is *in vivo* stability [9]. MBs that show *in*

vitro stability do not perform as well when continuously insonified because their shells are not designed to endure large deformations or blood flow-induced shear forces. The fast oscillations of MBs under an ultrasound field cause both leakage of the gas during expansion as well as loss of shell materials during compression, thus reducing their circulation time and usability [10].

Ultra-stable nanobubbles (NBs, 100-300 nm diameter) have been proposed as an alternative source of ultrasound contrast that provide synergistic improvements in resilience against deformations [11]–[13]. Moreover, NBs are sufficiently small to leave the vasculature but remain echogenic in the clinical frequency range (3-12 MHz) [14]. Lipid and surfactant-stabilized NBs can also exit the vasculature due to the enhanced permeability and retention (EPR) effect in the tumor vascular microenvironment. The EPR effect plays a crucial role in the increased accumulation of nanomedicines in the tumor parenchyma, targeting cancer cells directly. Unlike conventional MBs which remain in the tumor vasculature, NBs have the potential to become multifunctional theranostic agents, directly targeting cell-surface markers in the tumor tissue. Owing to their longer *in vivo* stability compared to MBs, NBs have been recently used for blood brain opening [12], contrast imaging of ovarian cancer [15] and shown to increase the cellular uptake and distribution of chemotherapeutic agents [11].

In this work, we investigate for the first-time radiation-enhanced nanobubble therapy as a means of increasing the tumoral cellular death compared to microbubbles. To elucidate the mechanism of action of NB-mediated radiation therapy on tumors, we propose the use of photoacoustic (PA) imaging. PA is an analog of ultrasonic imaging which relies on the use of laser illumination to generate acoustic waves from endogenous tissue chromophores such as hemoglobin inside red blood cells [16]. By sweeping the wavelength of illumination, PA imaging provides functional information about the oxygenation state of tumor blood vessels, while providing high resolution anatomical information about their spatial positioning [17]. Our group has shown that PA imaging can be used to monitor thermosensitive liposome treatments by identifying treatment responders as early as 30 minutes post-treatment [18], [19]. Here, we utilize the oxygen saturation as a variable to examine the mechanism of radiation-enhanced NB therapy.

II. MATERIALS AND METHODS

A. Animal model

Prostate cancer (PC3, 1×10^6 cells, American Type Culture Collection, Manassas, VA, USA) cells were inoculated into the upper right hind legs of CB-17 severe immunodeficiency (SCID) male mice (five- to six-week old, Charles River Laboratories International, Wilmington, MA, USA). Tumors were allowed to develop to a diameter of 8-10 mm from the initial time of induction.

B. Treatment protocol

A total of 58 mice were divided in the following six treatment groups:

- 1) Radiation only 8 Gy (n = 14)
- 2) Microbubbles + Ultrasound (MB+US, n = 8)
- 3) Nanobubbles + Ultrasound (NB+US, n = 5)
- 4) MB+US+8Gy (n = 12)
- 5) NB+US+8Gy (n = 5)
- 6) Untreated control (n = 14)

Definity MBs (mean diameter 3 μm , Lantheus Medical Imaging, N. Billerica, MA, USA) were activated by shaking for 45 seconds at 3000 rpm using the Lantheus Vialmix shaker device. The MBs were administered at a dose of 1.08×10^9 MBs in 90 μL volume via a tail vein injection.

Homemade NBs consisted of lipid shells with an octafluoropropane (C_3F_8) gas core and were formed via self-assembly driven by mechanical agitation [10]. Briefly, a mixture of lipids, 1,2-dipalmitoyl-sn-glycero-3-phosphoethanolamine (DPPE) (Corden Pharma Switzerland, Liestal, Switzerland), 1,2-dibehenoyl-sn-glycero-3-phosphocholine (DBPC), 1,2-distearoyl-sn-glycero-3-phosphoethanolamine-N-[met hoxyl (polyethylene glycol)-2000] (mPEG-DSPE), and 1,2-dipalmitoyl-sn-glycero-3-phosphate (DPPA) (Avanti Polar Lipids, Inc.) with a 2:6:1:2 ratio were dissolved in propylene glycol and glycerol in Phosphate Buffered Saline (PBS) solution. The solution was shaken with a C_3F_8 gas for 45 seconds using the VialMix to produce a mixture of micro and nanobubble solution. Nanobubbles were isolated via centrifugation and collected using a syringe. For the size and concentration measurement, the nanobubbles were diluted at 1:1000 v/v in PBS, and were measured using resonant mass measurement (Archimedes Malvern Panalytical, Malvern, UK) [13]. A total of 200 μL of NBs were injected via the tail vein per mouse. Fig. 1 shows the size distribution of a representative formulation of NBs used in this study. The mean diameter of the NBs was 205 ± 97 nm and the average concentration was measured to be 5.08×10^8 NBs per ml.

To deliver the ultrasound treatment, the mice were immersed in a 37 $^\circ\text{C}$ water bath. The tumor was positioned at the focus of a 500 kHz transducer (28.6 mm diameter, 85 mm focus, -6 dB zone of 31 mm, Valpey Fisher Inc., Hoptinkton, MA, USA, Cat# IL0509HP) [7]. Upon injection of the MBs or NBs, they were allowed to circulate for 5 minutes prior to exposing the tumors to 16 cycle tone bursts of 500 kHz frequency with a pulse repetition frequency of 3 kHz for 5

minutes. This resulted in 750 ms of exposure for an overall duty cycle of 0.25%.

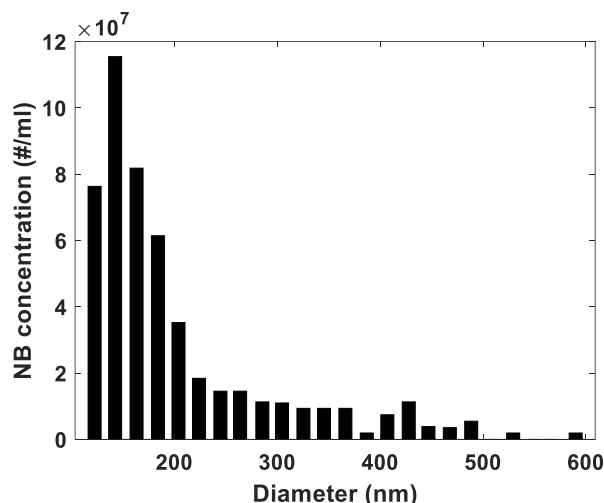


Fig. 1: Size distribution of NBs acquired with the Archimedes device.

For radiation treatments, the mouse torso was shielded with a lead sheet. The tumor region was exposed to radiation 3 hours after the bubble treatments through a confined circular aperture and a single dose of 8 Gy was delivered through a CP-160 cabinet X-radiator system (Faxitron Bioptics, LLC, Tucson, AZ, USA) at a rate of 200 cGy/minute.

C. Photoacoustic imaging protocol

All imaging was performed on the VevoLAZR small animal US/PA imaging device (Fujifilm-VisualSonics, Toronto, Canada). The system consisted of a 21 MHz, 256 element linear array probe coupled to an Nd:YAG laser delivered through a pair of optical fibers (30 mJ/pulse, 20 Hz pulse repetition frequency). Each mouse was laid in the prone position on a heated platform kept at 37 $^\circ\text{C}$. An external heating lamp was used to maintain constant physiological temperature and a rectal thermometer was used to monitor the animal's internal temperature.

All imaging was performed at 37 $^\circ\text{C}$ and the animals were anesthetized using 1.5% isoflurane for approximately 10 minutes per imaging timepoint. The tumor was positioned at the focus of the US/PA transducer (11 mm) and ultrasonic gel was used to provide acoustic coupling. The probe was mounted to a 3D stepper motor which enabled scanning of the entire tumor volume (80 μm step size). Co-registered 3D US and PA data were acquired at 750 nm and 850 nm at pre-treatment, 2h and 24h post-treatment (Fig. 2). Oxygen saturation ($s\text{O}_2$) was computed using a histogram-based approach developed by our group [18]. The mode of the histograms at each 2D slice for each imaging timepoint post-treatment was compared to the pre-treatment value and the untreated control group; it was reported as a percentage change relative to untreated control.

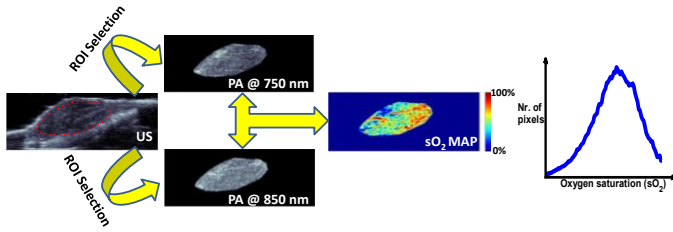


Fig. 2: PA imaging analysis workflow. The US image is used to anatomically segment the tumor and PA images acquired at 750 and 850 nm are used to generate sO_2 maps and the corresponding oxygenation histogram.

D. Histological analyses and relationship with PA imaging

Animals were sacrificed at 24 hours post-treatment. The tumors were harvested and fixed in 1% paraformaldehyde overnight prior to embedding in paraffin blocks; cross sections were cut from a representative region in the center of the tumor. Standard hematoxylin and eosin staining were obtained in addition to TUNEL for assessing the degree of apoptotic cellular death. All quantification analysis was performed using the HALO[®] image analysis platform (Indica Labs, Albuquerque, NM, USA). The change in the percentage of tumor cell death relative to the untreated control group was computed for each treatment group. The average TUNEL change from control at 24 hours was correlated with the change in the tumor sO_2 .

III. RESULTS AND DISCUSSION

A. Tumor oxygenation as a function of treatments

Fig. 3 shows the change in tumor oxygenation relative to untreated control for all the treatments summarized in section II.B. The sO_2 at 2- and 24-hours post-treatment was compared to the untreated control mice. The radiation therapy treatment shows an increase in the tumor oxygenation, observed as early as 2 hours post-treatment. While the exact mechanism behind these observations is unclear, it is possible that there is a decrease in cellular metabolism and oxygen consumption in tumors following radiation treatments [20]. The acute inflammatory response that is triggered by radiation-induced cellular damage may increase the tumor perfusion, thus increasing the oxyhemoglobin concentration within the tumor.

The MB+US treatments have been shown to induce vascular damage by targeting the endothelial cells lining the tumor blood vessels. The inertial cavitation of the MBs confined to the tumor vasculature causes the release of ceramide, subsequently leading to endothelial cell apoptosis [8]. The disruption of the vessel lining causes a vascular shut down into the tumor. PA imaging is sensitive to a decreased supply of oxyhemoglobin, due to the decreased blood flow and reduction of the heme group to deoxyhemoglobin due to lack of oxygen. This causes the oxygenation of the red blood cells to decrease, leading to an approximately 8% reduction in sO_2 at 24 hours post-treatment. The NB+US treatment causes the tumor sO_2 to decrease by nearly 12% at the same timepoint. This suggests that the NB and US exposure impacts the tumor vasculature similarly to MBs.

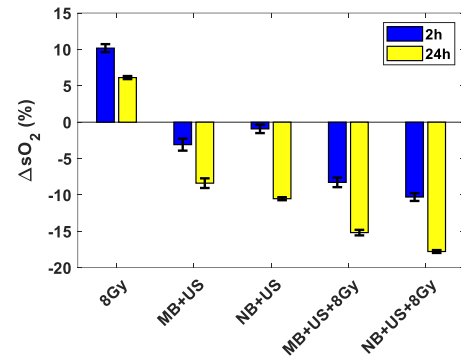


Fig. 3: Change in tumor oxygenation (ΔsO_2) for each treatment relative to the untreated control group. Each bar represents the percentage difference from both imaging timepoints relative to pre-treatment for the 3D tumor volume, for all mice.

When combined with radiation, the MB and NB treatments decrease in tumor oxygenation is further amplified. The largest decrease occurred for NB+US+8Gy at 24 hours post-treatment (18%). Even at 2 hours post-exposure, the decrease is still 10% larger than the NB+US treatment. Moreover, the combined NB treatment resulted in 5% more sO_2 decrease compared to the MB counterpart.

B. Histological measurements of cell death

Histological analysis of the tumors post-treatment allows us to examine the mechanism of action of each therapy combination. Fig. 4a shows representative images of TUNEL staining for an untreated control and NB+US+8Gy treated mouse. There is a notable increase in the brown TUNEL staining in the treatment group compared to control, similar to what is observed for MB+US treatments [7], [8]. Quantification of the apoptosis stain (Fig. 4b) reveals more than 2-fold higher degree of cell death for the NB+US group compared to the MB+US counterpart. This suggests that the NBs are more effective at targeting the tumor cells, most likely due to their ability to extravasate in the tumor interstitium [10]. The combined NB+US+8Gy exhibited on average 40% more cell death than the untreated control at 24 hours post treatment. The increased degree of cell death in the NB group could also be due to the largest changes in tumor oxygenation that occur from the cavitation-induced vascular disruption of the NBs.

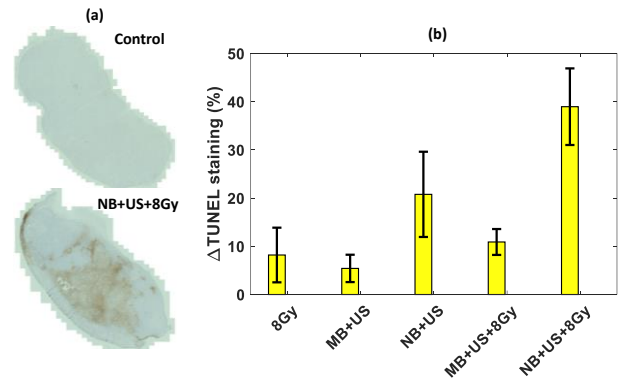


Fig. 4: (a) Representative TUNEL histology images showing increased cell death in a NB-treated tumor relative to control. (b) Changes in the TUNEL staining of all treated tumors. The TUNEL staining area is defined in the context of the overall tumor area.

C. Relationship between histology and PA imaging

To further understand on the mechanism of action for MB/NB-enhancements of radiation therapy and aid in the interpretation of PA imaging findings, we examined the relationship between the two. Fig. 5 shows how the change in tumor oxygenation (ΔsO_2) impacts the degree of tumor cell death ($\Delta TUNEL$ staining). The tumors that exhibit the largest degree of cell death are also the ones with the largest drop in oxygenation, namely the NB+US+8Gy (~18%). In addition to the radiation-induced damage to the tumor cells, it might be possible that due to the larger number of NBs confined in the tumor vasculature, occlusion of the vessels occurred in the treatment (in addition to the endothelial disruption). This could contribute to the decreased vascularity of treated tumors, which leads to a drop in tumor oxygenation (Fig. 3). These findings suggest that the NBs affect the integrity of the endothelial cells, extravasating into the tumor interstitium where they directly target cancer cells, inducing cellular death. Our results show approximately 20% more cell death when NBs are used in conjunction with radiation compared to the conventional MBs.

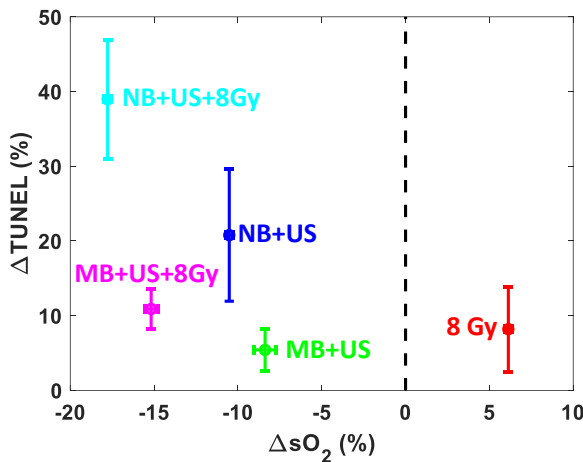


Fig. 5: Relationship between tumor cellular death (measured through TUNEL staining) and tumoral oxygenation (measured with PA imaging). The changes in each parameter are compared against the untreated control mice.

IV. CONCLUSIONS

In this work we show for the first time the therapeutic capabilities of nanobubbles as enhancers of radiation therapy of tumors. The newly developed NB treatments appears to induce significant cellular death within the tumor which may be a result of disruption of the tumor vasculature. These results suggest that enhancement of radiation treatments through NBs is a feasible type of vascular targeted therapy.

ACKNOWLEDGMENT

This research was undertaken, in part, through grants obtained from the Terry Fox Research Institute, Natural Sciences and Engineering Council of Canada and the National Institutes of Health. E. Hysi is supported through a Vanier Canada Graduate Scholarship and M. Fadhel is supported through an NSERC Alexander Graham Bell Graduate Scholarship.

REFERENCES

- [1] R. Gramiak and P. M. Shah, "Echocardiography of the aortic root," *Invest. Radiol.*, vol. 3, no. 5, pp. 356–366, Oct. 1968.
- [2] S. Qin, C. F. Caskey, and K. W. Ferrara, "Ultrasound contrast microbubbles in imaging and therapy: physical principles and engineering," *Phys. Med. Biol.*, vol. 54, no. 6, pp. R27–R57, Mar. 2009.
- [3] H. Moon *et al.*, "Therapeutic Ultrasound Contrast Agents for the Enhancement of Tumor Diagnosis and Tumor Therapy," *J. Biomed. Nanotechnol.*, vol. 11, no. 7, pp. 1183–1192, Jul. 2015.
- [4] X. Liang, Y. Xu, C. Gao, Y. Zhou, N. Zhang, and Z. Dai, "Ultrasound contrast agent microbubbles with ultrahigh loading capacity of camptothecin and floxuridine for enhancing tumor accumulation and combined chemotherapeutic efficacy," *NPG Asia Mater.*, vol. 10, no. 8, pp. 761–774, Aug. 2018.
- [5] C. Holland, "Ultrasound Contrast Agents Accelerate Sonothrombolysis," *Ultrasound Med. Biol.*, vol. 41, no. 4, p. S94, Apr. 2015.
- [6] K. Hynynen, N. McDannold, N. Vykhodtseva, and F. A. Jolesz, "Noninvasive MR imaging-guided focal opening of the blood-brain barrier in rabbits," *Radiology*, vol. 220, no. 3, pp. 640–646, Sep. 2001.
- [7] G. J. Czarnota *et al.*, "Tumor radiation response enhancement by acoustical stimulation of the vasculature," *Proc. Natl. Acad. Sci. U. S. A.*, vol. 109, no. 30, pp. E2033–E2041, Jul. 2012.
- [8] A. A. Al-Mahrouki, S. Iradji, W. T. Tran, and G. J. Czarnota, "Cellular characterization of ultrasound-stimulated microbubble radiation enhancement in a prostate cancer xenograft model," *Dis. Model. Mech.*, vol. 7, no. 3, pp. 363–372, Mar. 2014.
- [9] H. Wu, E. C. Abenojar, R. Perera, A. C. De Leon, T. An, and A. A. Exner, "Time-intensity-curve Analysis and Tumor Extravasation of Nanobubble Ultrasound Contrast Agents," *Ultrasound Med. Biol.*, vol. 45, no. 9, pp. 2502–2514, Sep. 2019.
- [10] A. de Leon *et al.*, "Contrast enhanced ultrasound imaging by nature-inspired ultrastable echogenic nanobubbles," *Nanoscale*, vol. 11, no. 33, pp. 15647–15658, Sep. 2019.
- [11] P. Nittayacharn, H.-X. Yuan, C. Hernandez, P. Bielecki, H. Zhou, and A. A. Exner, "Enhancing Tumor Drug Distribution With Ultrasound-Triggered Nanobubbles," *J. Pharm. Sci.*, vol. 108, no. 9, pp. 3091–3098, Sep. 2019.
- [12] C. Bing *et al.*, "Characterization of different bubble formulations for blood-brain barrier opening using a focused ultrasound system with acoustic feedback control," *Sci. Rep.*, vol. 8, no. 1, pp. 1–12, May 2018.
- [13] C. Hernandez *et al.*, "Sink or float? Characterization of shell-stabilized bulk nanobubbles using a resonant mass measurement technique," *Nanoscale*, vol. 11, no. 3, pp. 851–855, Jan. 2019.
- [14] A. J. Sojahrood, L. Nieves, C. Hernandez, A. Exner, and M. C. Kolios, "Theoretical and experimental investigation of the nonlinear dynamics of nanobubbles excited at clinically relevant ultrasound frequencies and pressures: The role of lipid shell buckling," in *2017 IEEE International Ultrasonics Symposium (IUS)*, 2017, pp. 1–1.
- [15] Y. Gao *et al.*, "Ultrasound molecular imaging of ovarian cancer with CA-125 targeted nanobubble contrast agents," *Nanomedicine Nanotechnol. Biol. Med.*, vol. 13, no. 7, pp. 2159–2168, Oct. 2017.
- [16] L. V. Wang and S. Hu, "Photoacoustic tomography: in vivo imaging from organelles to organs," *Science*, vol. 335, no. 6075, pp. 1458–1462, Mar. 2012.
- [17] S. Manohar and D. Razansky, "Photoacoustics: a historical review," *Adv. Opt. Photonics*, vol. 8, no. 4, p. 586, Dec. 2016.
- [18] J. P. May, E. Hysi, L. A. Wirtzfeld, E. Undzys, S.-D. Li, and M. C. Kolios, "Photoacoustic Imaging of Cancer Treatment Response: Early Detection of Therapeutic Effect from Thermosensitive Liposomes," *PLoS One*, vol. 11, no. 10, p. e0165345, 2016.
- [19] E. Hysi, L. A. Wirtzfeld, J. P. May, E. Undzys, S.-D. Li, and M. C. Kolios, "Photoacoustic signal characterization of cancer treatment response: Correlation with changes in tumor oxygenation," *Photoacoustics*, vol. 5, pp. 25–35, Mar. 2017.
- [20] L. J. Rich and M. Seshadri, "Photoacoustic monitoring of tumor and normal tissue response to radiation," *Sci. Rep.*, vol. 6, p. 21237, Feb. 2016.